The Astrophysical Journal, 885:18 (9pp), 2019 November 1 https://doi.org/10.3847/1538-4357/ab4595

An Evolving Broad Iron Line from the First Galactic Ultraluminous X-Ray Pulsar Swift J0243.6+6124

Gaurava K. Jaisawal[1], Colleen A. Wilson-Hodge[2], Andrew C. Fabian[3], Sachindra Naik[4], Deepto Chakrabarty[5], Peter Kretschmar[6], David R. Ballantyne[7], Renee M. Ludlam[8,9,18], Jérôme Chenevez[1], Diego Altamirano[10], Zaven Arzoumanian[11], Felix Fürst[6], Keith C. Gendreau[11], Sebastien Guillot[12,13], Christian Malacaria[14,15,19], Jon M. Miller[8], Abigail L. Stevens[8,16,20], and Michael T. Wolff[17]

[1] National Space Institute, Technical University of Denmark, Elektrovej 327-328, DK-2800 Lyngby, Denmark; gaurava@space.dtu.dk
[2] ST12 Astrophysics Branch, NASA Marshall Space Flight Center, Huntsville, AL 35812, USA
[3] Institute of Astronomy, University of Cambridge, Madingley Road, Cambridge CB3 0HA, UK
[4] Astronomy and Astrophysics Division, Physical Research Laboratory, Navrangapura, Ahmedabad—380009, Gujarat, India
[5] MIT Kavli Institute for Astrophysics and Space Research, Massachusetts Institute of Technology, Cambridge, MA 02139, USA
[6] European Space Astronomy Centre (ESAC), Science Operations Departement, E-28692 Villanueva de la Cañada, Madrid, Spain
[7] Center for Relativistic Astrophysics, School of Physics, Georgia Institute of Technology, 837 State Street, Atlanta, GA 30332-0430, USA
[8] Department of Astronomy, University of Michigan, 1085 South University Avenue, Ann Arbor, MI 48109-1107, USA
[9] Cahill Center for Astronomy and Astrophysics, California Institute of Technology, Pasadena, CA 91125, USA
[10] Physics & Astronomy, University of Southampton, Southampton, Hampshire SO17 1BJ, UK
[11] Astrophysics Science Division, NASA's Goddard Space Flight Center, Greenbelt, MD 20771, USA
[12] CNRS, IRAP, 9 avenue du Colonel Roche, BP 44346, F-31028 Toulouse Cedex 4, France
[13] Université de Toulouse, CNES, UPS-OMP, F-31028 Toulouse, France
[14] NASA Marshall Space Flight Center, NSSTC, 320 Sparkman Drive, Huntsville, AL 35805, USA
[15] Universities Space Research Association, NSSTC, 320 Sparkman Drive, Huntsville, AL 35805, USA
[16] Department of Physics & Astronomy, Michigan State University, 567 Wilson Road, East Lansing, MI 48824, USA
[17] Space Science Division, U.S. Naval Research Laboratory, Washington, DC 20375, USA
Received 2019 June 3; revised 2019 September 15; accepted 2019 September 16; published 2019 October 25

Abstract

We present a spectral study of the ultraluminous Be/X-ray transient pulsar Swift J0243.6+6124 using *Neutron Star Interior Composition Explorer* (*NICER*) observations during the system's 2017–2018 giant outburst. The 1.2–10 keV energy spectrum of the source can be approximated with an absorbed cutoff power-law model. We detect strong, luminosity-dependent emission lines in the 6–7 keV energy range. A narrow 6.42 keV line, observed in the sub-Eddington regime, is seen to evolve into a broad Fe-line profile in the super-Eddington regime. Other features are found at 6.67 and 6.97 keV in the Fe-line complex. An asymmetric broad-line profile, peaking at 6.67 keV, is possibly due to Doppler effects and gravitational redshift. The 1.2–79 keV broadband spectrum from *Nuclear Spectroscopic Telescope Array* (*NuSTAR*) and *NICER* observations at the outburst peak is well described by an absorbed cutoff power law plus multiple Gaussian lines and a blackbody component. Physical reflection models are also tested to probe the broad iron-line feature. Depending on the mass accretion rate, we found emission sites that are evolving from ∼5000 km to a range closer to the surface of the neutron star. Our findings are discussed in the framework of the accretion disk and its implication on the magnetic field, the presence of optically thick accretion curtain in the magnetosphere, jet emission, and the massive, ultrafast outflow expected at super-Eddington accretion rates. We do not detect any signatures of a cyclotron absorption line in the *NICER* or *NuSTAR* data.

Unified Astronomy Thesaurus concepts: Accretion (14); High mass X-ray binary stars (733); Neutron stars (1108); Pulsars (1306)

1. Introduction

Fluorescent emission lines of iron have been ubiquitously observed at energies in the 6.4–6.9 keV range in the spectra of various classes of astrophysical sources, such as X-ray binaries and active galactic nuclei (for reviews, see Fabian et al. 2000; Miller 2007; Bhattacharyya 2010). X-ray "reflection" from an accretion disk or stellar wind is known to produce narrow Fe emission features. As the line-emitting region approaches a compact object, Doppler and relativistic effects broaden the Fe line (Fabian et al. 1989). An asymmetric, redshifted profile emerges in the spectrum, due to strong relativistic effects in the vicinity of the central X-ray source. Hence, understanding the characteristic properties of such broadened emission lines serves to probe the dynamics of the accretion flow and the gravitational redshift near the compact object. Asymmetric, broad iron profiles are known in active galactic nuclei as well as low mass X-ray binaries with black hole or neutron star accretors (see, e.g., Miller 2006, 2007; Bhattacharyya 2010). We study the Fe emission in the case of a high-mass X-ray binary pulsar, Swift J0243.6+6124, using *Neutron Star Interior Composition Explorer* (*NICER*) observations.

The X-ray transient Swift J0243.6+6124 was discovered with the Neil Gehrels *Swift* Observatory in 2017 October during the onset of a strong outburst (Cenko et al. 2017; Kennea et al. 2017). Detection of 9.8 s pulsations identified the source as an X-ray pulsar (Bahramian et al. 2017; Jenke & Wilson-Hodge 2017; Kennea et al. 2017; Jaisawal et al. 2018). Swift J0243.6+6124 harbors a highly magnetized neutron star

[18] Einstein Fellow.
[19] NASA Postdoctoral Fellow.
[20] NSF Astronomy & Astrophysics Postdoctoral Fellow.

($\leqslant 10^{13}$ G; Tsygankov et al. 2018; Wilson-Hodge et al. 2018), accreting from a massive optical companion of Oe- or early Be-type (Bikmaev et al. 2017). The constraint on its magnetic field is obtained tentatively using the independent methods based on the "propeller" luminosity from the source flux evolution (Tsygankov et al. 2018), measuring the critical luminosity from hardness ratios, and also from the detected quasi-periodic oscillations in *NICER* data (Wilson-Hodge et al. 2018). The system has a 27.6 days eccentric ($e \approx 0.1$) orbit (Doroshenko et al. 2018; Wilson-Hodge et al. 2018), and is located at a distance of ≈7 kpc based on *Gaia* DR2 as described in Wilson-Hodge et al. (2018).

The 2017 giant outburst from the system lasted approximately five months, with a peak X-ray luminosity $\sim 10^{39}$ erg s^{-1}, which exceeds the Eddington limit of a neutron star (Tsygankov et al. 2018; Wilson-Hodge et al. 2018). This luminosity classified the source as an ultraluminous X-ray (ULX) pulsar, the very first detected inside our Galaxy. ULXs are powerful, off-nuclear (extragalactic), point-like sources, emitting at a luminosity $\geqslant 10^{39}$ erg s^{-1} (see Kaaret et al. 2017 for a review). A few of them are pulsars with spin periods in the range ∼1–30 s (e.g., Bachetti et al. 2014; Fürst et al. 2016; Israel et al. 2017a) and magnetic fields in the range 10^{11}–10^{13} G (King & Lasota 2019). A much stronger multipolar field strength is also reported in ULX pulsars (see, e.g., Israel et al. 2017a, 2017b). It remains unclear what powers these sources. A possible explanation comes from a combination of super-Eddington accretion and geometric collimation effect (King 2009; Middleton et al. 2015). Some of the ULXs are also known to produce relativistic jets (Kaaret et al. 2003 and references therein).

A radio counterpart of Swift J0243.6+6124 was detected in the 6 and 22 GHz bands using the Karl G. Jansky Very Large Array (VLA; van den Eijnden et al. 2018). The analysis suggested that the pulsar launches a jet at high-mass accretion rate. Current understanding favors the jet outflows from black holes (in the low/hard state) or weakly magnetized neutron stars in X-ray binaries (Fender 2006), while the absence of jet formation in accreting pulsars is thought to be due to strong magnetic fields of order $\sim 10^{12}$ G, as well as their slower rotation (Massi & Kaufman Bernadó 2008; Parfrey et al. 2016). The existence of such strong field is expected to hinder the magneto-centrifugal jet driving mechanism by simply truncating the accretion disk far away from the neutron star.

The observed radio emission from Swift J0243.6+6124 evolved across the 2017 outburst. It followed a radio-X-ray correlation, $L_{\rm radio} \propto L_{\rm x}^{0.54\pm0.16}$, consistent with both black hole and neutron star X-ray binaries. Further VLA monitoring found that the jet emission turned on and off within days (van den Eijnden et al. 2019). The jet emission also appeared when the pulsar rebrightened in fainter X-ray outbursts in 2018 March and May. The jet persisted in these later observations only when the X-ray luminosity was $\geqslant 4 \times 10^{36}\,(D/7\,{\rm kpc})^2$ erg s^{-1}, and was equally radio bright as at the peak of the 2017 outburst (van den Eijnden et al. 2019).

Using *NICER* (Gendreau et al. 2012), we explore the spectral characteristics of the pulsar Swift J0243.6+6124 during the 2017–2018 strong outburst. This paper mainly focuses on the detection of a broad, asymmetric iron emission line and its evolution across the sub- and super-Eddington regimes. We describe the observations and analysis in Section 2. The results and discussion are presented in Sections 3 and 4, respectively.

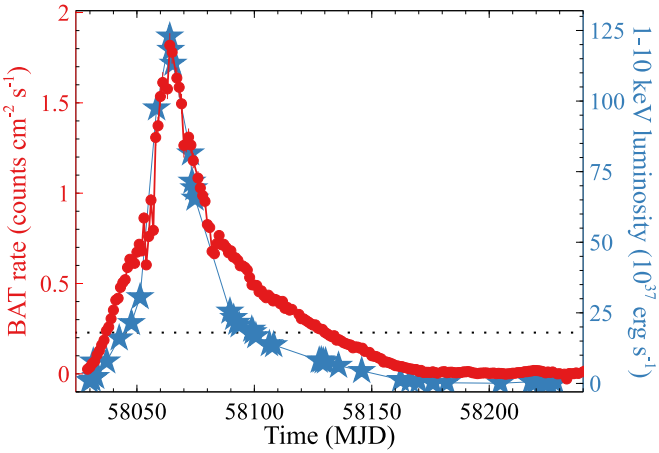

Figure 1. Outburst monitoring light curve of Swift J0243.6+6124 from *Swift*/BAT in the 15–50 keV range (solid dots; Krimm et al. 2013). The 1–10 keV unabsorbed luminosity light curve (solid stars) is also shown from *NICER* observations between 2017 October 3 (MJD 58029) and 2018 April 20 (MJD 58228). The pulsar was extremely bright at the outburst peak, reaching 9 Crab intensity in the BAT band; for reference, 1 Crab represents 0.220 counts cm^{-2} s^{-1} in this band. The horizontal dotted line in the figure represents the Eddington luminosity of a 1.4 $M_\odot$ neutron star.

2. Observations and Data Analysis

2.1. NICER

The *NICER* X-ray timing instrument (XTI; Gendreau et al. 2012, 2016) is a nonimaging, soft X-ray telescope installed on the International Space Station in 2017 June. The XTI consists of an array of 56 co-aligned concentrator optics, each associated with a silicon drift detector (Prigozhin et al. 2012), together operating in the 0.2–12 keV band. The XTI provides high time resolution of ∼100 ns (rms) and spectral resolution of ≈85 eV at 1 keV. It has a field of view of ≈30 arcmin^2 in the sky. The effective area of *NICER* is ≈1900 cm^2 at 1.5 keV, with 52 active detectors.

NICER has continued monitoring Swift J0243.6+6124 since its discovery in 2017 October by covering numerous epochs of the outburst (Figure 1). Initial results from these observations were reported in Wilson-Hodge et al. (2018). Here, we present evidence of an evolving iron line using the same data sets (ObsIDs 1050390101–1050390160) between 2017 October and 2018 April. A detailed observation log can be found in Table 1 of Wilson-Hodge et al. (2018).

Data were reduced using HEASOFT version 6.24, NICERDAS version 2018-04-24_V004, and the calibration database (CalDB) version 20180711. We excluded events from the South Atlantic Anomaly region; other filtering criteria such as elevation angle >30° from the Earth limb, pointing offset $\leqslant 54''$, offset from the bright Earth >40°, and also COR_SAX $\geqslant 4$ to remove the high charged particle background regions were used to screen the data. Here, COR_SAX is the magnetic cutoff rigidity, in GeV/c. From the resulting good time intervals, final spectral products were created with XSELECT. We used blank-sky regions (e.g., field *RXTE*-6; Jahoda et al. 2006) to estimate the background corresponding to our observations.

2.2. NuSTAR

Following the source discovery, the *Nuclear Spectroscopic Telescope Array* (*NuSTAR*; Harrison et al. 2013) monitored the

pulsar at various epochs during the 2017–2018 outburst. We note that these observations have already been used for spectral studies (Jaisawal et al. 2018; Tao et al. 2019). In this paper, we focus on quasi-simultaneous *NuSTAR* and *NICER* observations from the outburst peak to study the broadband X-ray spectrum. The effective exposure of the *NuSTAR* pointing on 2017 October 31 (ObsID 90302319004) is 1293 s, while the *NICER* observation took place on 2017 November 1 for an effective exposure of 3406 s (ObsID 1050390113).

Standard methods were adopted for *NuSTAR* data analysis.[21] Before reprocessing, we set an additional keyword "statusexpr" to "STATUS==b0000xx00xx0xx000" in `nupipeline` to retain events that might have been flagged as "hot" or "flickering" due to the high count rate of the source >100 counts s^{-1}. Data from both focal plane modules, FPMA and FPMB, were used in our analysis. We considered a source region of 150″ for the spectral extraction, while the background is measured from a source-free region with a similar radius. The final products were generated using `nuproduct` task.

3. Spectral Analysis and Results

The spectrum was analyzed using XSPEC version 12.10.0 (Arnaud 1996) along with response matrices and effective area files (version 1.02 for *NICER*). The *NICER* spectrum suffers from instrumental residuals in the Si (1.7–2.1 keV) and Au (2.2–2.3 keV) bands for bright sources like Swift J0243.6+6124. These features are prominent due to the high sensitivity of *NICER* and calibration uncertainties. To minimize the effects of the residuals, we adopted a Crab-correction technique that exploits the featureless power-law spectrum observed from the Crab Nebula. In this approach, the target spectrum is renormalized by a residual template created by dividing the observed Crab Nebula spectrum by a simulated Crab spectrum (see, e.g., Ludlam et al. 2018 and Wilson-Hodge et al. 2018 for details). The Crab-corrected spectrum of Swift J0243.6+6124 is fitted after adding a 1.5% systematic error in the 1.2–10 keV range. The data below 1.2 keV are ignored because of calibration uncertainties and strong residuals at 1 keV.

3.1. Evolution of Iron Lines

To study the evolution of the Fe-line complex, we fitted each of the *NICER* observations with an absorbed cutoff power-law model. This empirical model is commonly employed to describe the continuum spectrum of accretion-powered X-ray pulsars (White et al. 1983; Bildsten et al. 1997). A similar model with an additional blackbody component has successfully reproduced the 3–79 keV *NuSTAR* spectrum of Swift J0243.6+6124 at a low luminosity (Jaisawal et al. 2018). Considering the limited energy band up to 10 keV, the cutoff power-law model, using the `tbabs` absorption model with the abundance table of Wilms et al. (2000), is preferred to fit the *NICER* spectrum.

Figure 2 shows the spectral ratio (between the source spectrum and corresponding best-fit continuum model) from some of the representative *NICER* observations at several epochs of the X-ray outburst. The Fe-line structure is clearly visible in the residuals. A narrow emission line at ≈6.4 keV was detected in the spectrum at lower source luminosity (e.g., ObsID 55). As the intensity increased, this feature became broader in energy, and an additional emission component at ≈6.97 keV appeared. An emission line at ≈6.67 keV also becomes apparent at higher luminosity (see, e.g., ObsID 24). At even higher luminosity, the line profile transformed into a broad, double-peaked shape with almost equal contribution from the 6.4 and 6.67 keV lines at a source luminosity of $\approx 25 \times 10^{37}$ erg s^{-1} (Figure 2). Finally, the emission from 6.67 keV dominated the line complex at a luminosity $\geqslant 69 \times 10^{37}$ erg s^{-1}. A broad-line profile with a strong red wing was also observed in the 4–8 keV range in the super-Eddington regime. This is the first time that such a broad asymmetric Fe line has been detected in a strongly magnetized accreting neutron star (see also Miller et al. 2018 and Kara et al. 2019 for *NICER* spectral capabilities in the Fe band). The 6.4 keV line is identified as a fluorescent line from neutral or weakly ionized Fe, whereas the 6.67 and 6.98 keV lines originate from highly ionized He-like and H-like Fe ions, respectively.

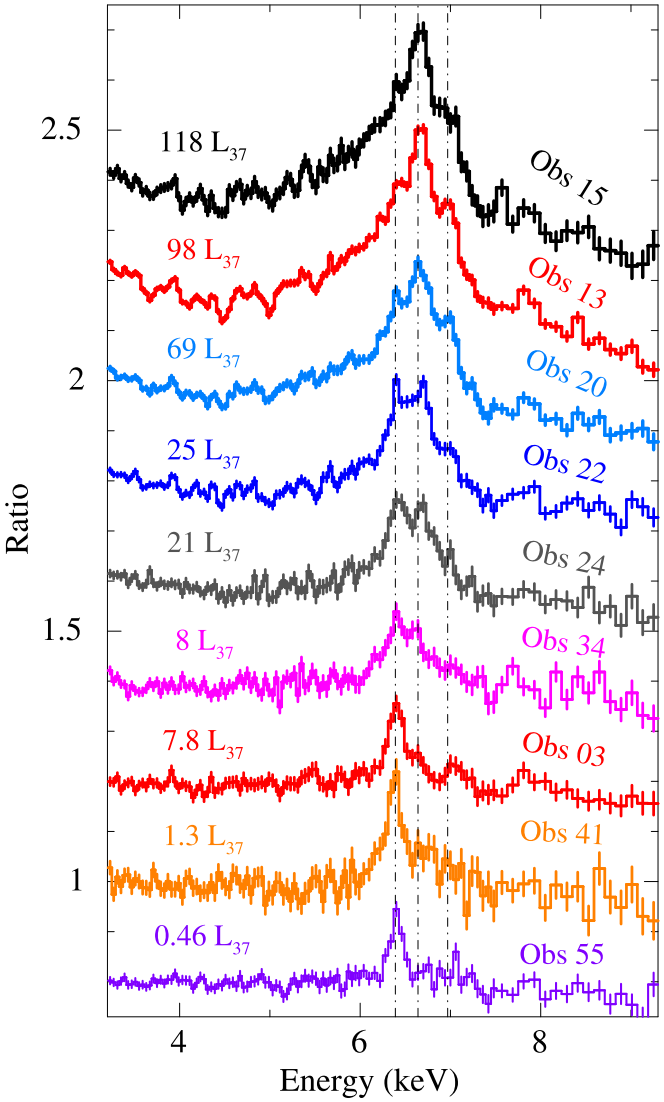

Figure 2. Ratio of *NICER* data to the continuum model (scaled arbitrarily) obtained by fitting 1.2–10 keV energy spectra of Swift J0243.6+6124 with an absorbed cutoff power-law model. These are arranged in order of increasing luminosity. L_{37} stands for unabsorbed luminosity in units of 10^{37} erg s^{-1}. Observation IDs (10503901xx) are also shown as labels. Three emission lines in the 6–7 keV range are detected at 6.4, 6.67, and 6.98 keV energies (vertical dashed–dotted lines).

[21] https://heasarc.gsfc.nasa.gov/docs/nustar/analysis/nustar_swguide.pdf

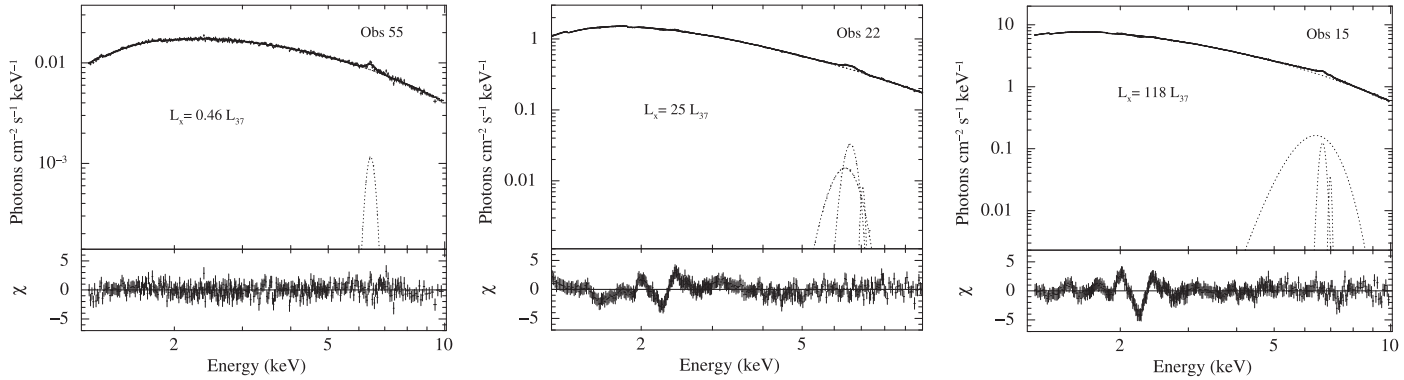

Figure 3. 1.2–10 keV energy spectrum of Swift J0243.6+6124 with *NICER* at three representative luminosities after fitting with an absorbed cutoff power-law model plus Gaussian components (top panel). A single narrow line at ≈6.4 keV was required at the lower luminosity (left; Obs 55). Two emission lines were clearly detected in the Fe band at higher luminosity (middle; Obs 22). The energy spectrum at the super-Eddington state is described using an absorbed cutoff power-law model with three line components (right; Obs 15). Spectral residuals corresponding to the best-fitting models are shown in the bottom panels. The feature observed in the 2–3 keV range of the residuals (middle and right panels) is possibly instrumental in origin.

We modeled the Fe-line structure by adding Gaussian line components to our absorbed cutoff power-law model. For low source luminosities, Gaussian components were added in the 6–7 keV range to fit the observed narrow lines (e.g., left and middle panels of Figure 3). By contrast, a significantly broad line from the ultraluminous phase was modeled using three Gaussian functions, keeping their central energies fixed at 6.4, 6.7, and 7.0 keV (e.g., right panel of Figure 3). The inclusion of the emission components in the spectral model improved the overall fit with a reduced χ^2 ⩽1.5 in each case and provided a statistical improvement of $>6\sigma$ in the fitting. The statistical significance of the emission line is determined by using the *XSPEC* script `simftest` that estimate the F-test probability through Monte Carlo simulations (see also Protassov et al. 2002).

We employed the `cflux` model to compute the 1–10 keV unabsorbed flux. The Fe-line fluxes are calculated separately, combining all individual Gaussian components in the model spectra. The estimated fluxes are also corrected for detector deadtime (see Section 3.1 of Wilson-Hodge et al. 2018 for a discussion on *NICER* deadtime corrections for bright sources). The 1–10 keV source luminosity is calculated assuming a distance of 7 kpc. Figure 4 shows the variation between luminosity and the line width of each of the Fe-components. A clear evolution from a narrow to broad emission line is detected for the 6.4 keV feature in sub- and super-Eddington domains, respectively. However, the 6.67 and 6.98 keV lines are remain narrow above the Eddington luminosity. The correlation between the source luminosity and the observed Fe-line flux is also shown in Figure 5. We found that the Fe-line flux strongly traces the source intensity over more than three orders of magnitude. We focus on the results from the iron emission line in this paper. A detailed discussion of all other parameters will follow in a future publication.

We also explored the correlation between Fe-line emission and the radio flux density as observed with VLA (Figure 6). The radio data used here are taken from van den Eijnden et al. (2018) and van den Eijnden et al. (2019). The VLA observations were quasi-simultaneous to *NICER* pointings (ObsIDs 1050390105, 1050390116, 1050390118, 1050390122, 1050390134, and 1050390143) between 2017 October and 2018 February. From Figure 6, it is clear that the Fe-line flux shows a positive correlation with radio flux density in the high-flux regime. This pattern is possibly changed at lowest Fe-line flux (one data point

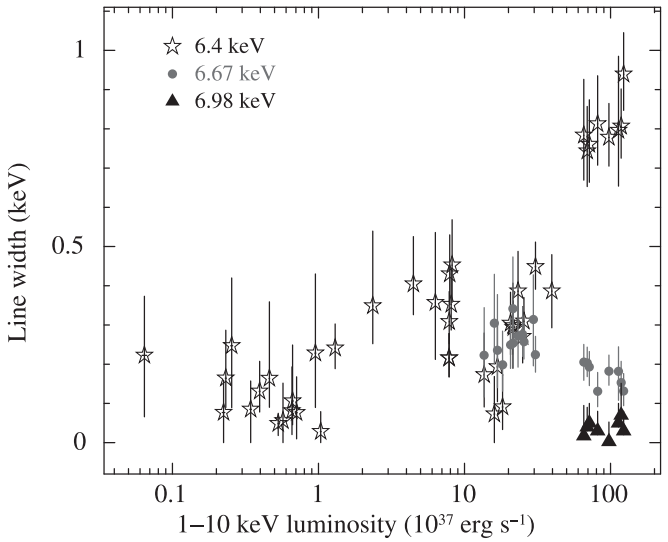

Figure 4. Luminosity evolution of line width for 6.4, 6.67, and 6.98 keV emission components during the outburst.

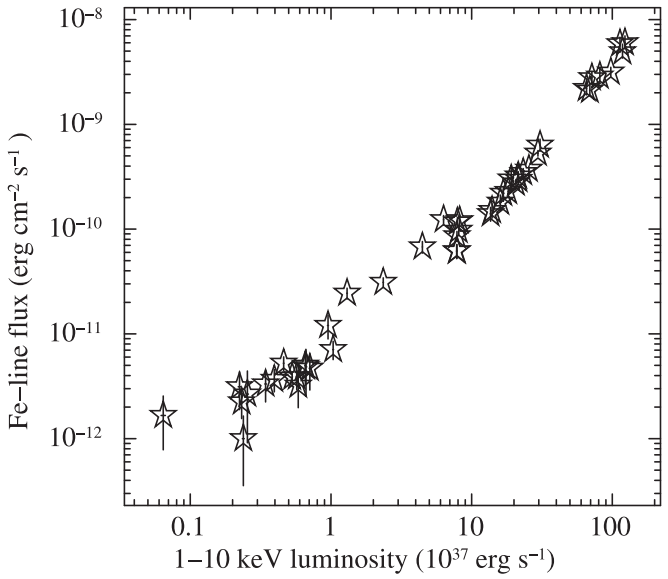

Figure 5. Variation in the 1–10 keV unabsorbed luminosity with Fe-band flux obtained from fitting *NICER* data with a cutoff power-law model. The line flux traces the source intensity for more than three orders of magnitude.

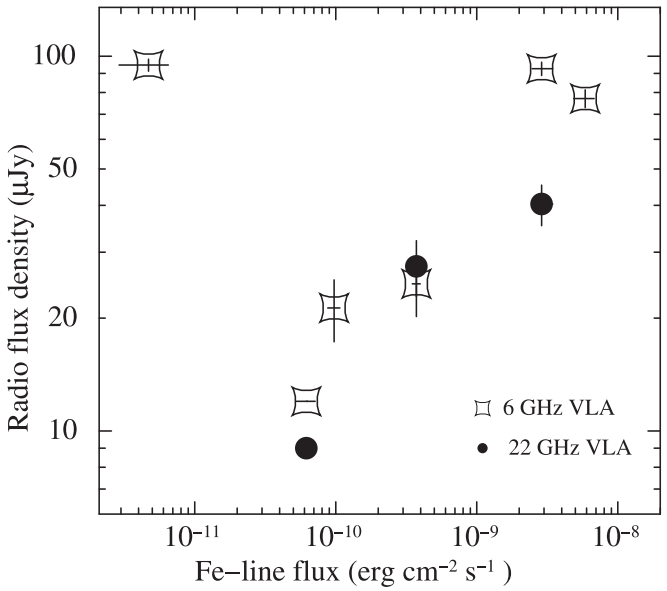

Figure 6. Observed iron-band flux with radio flux densities at two frequencies.

at 6 GHz). The observed variation is consistent with the radio-X-ray luminosity relation, in general, reported by van den Eijnden et al. (2018, 2019), where the source followed a positive trend with radio measurement at high-mass accretion rate. A change in the correlation was observed at lower luminosity due to the detection of jet emission similar in brightness to that at the outburst peak (van den Eijnden et al. 2018, 2019).

3.2. *Broadband Spectroscopy with* NICER *and* NuSTAR

We used data from quasi-simultaneous *NICER* and *NuSTAR* observations at an epoch close to the outburst peak to understand the broadband emission characteristics of Swift J0243.6+6124 in the super-Eddington domain. The 1.2–79 keV energy spectrum was first fitted with an absorbed cutoff power-law (Cutoff) with a blackbody (BB) component for excess emission in the soft X-rays (Jaisawal et al. 2018). As expected, the above model yielded a statistically unacceptable fit due to a strong, asymmetric, broad emission line complex in the 4–8 keV range (second panel of Figure 7). The goodness of the fit is $\chi^2_\nu = \chi^2/\nu = 5.33$, where ν indicates the number of degrees of freedom (dof). This also produced strong residuals or spectral curvatures at both ends of the 4–8 keV band (see second panel of Figure 7). Recently, Tao et al. (2019) approximated the same *NuSTAR* data in 3–79 keV with a complex model. The authors used a cutoff power-law continuum along with three blackbody components, at 0.57, 1.46, and 4.5 keV temperatures. The thermal blackbody at 0.57 keV (with a radius of 120 km) is interpreted as the photospheric emission from the optically thick outflow, while the components at 1.46 keV with radius 20 km and 4.5 keV with radius 1.4 km are explained as a temperature gradient from the top to the base of the accretion column, respectively (Tao et al. 2019). A marginal detection of an asymmetric Fe line was also reported in the above work.

Combining the *NuSTAR* data with the high sensitivity and soft X-ray coverage of *NICER*, the 1.2–79 keV energy spectrum was fitted using a Cutoff+BB model along with three Gaussian functions of fixed central energies at 6.4, 6.7, and 7.0 keV (see Table 1). An edge feature at ≈7.1 keV is also

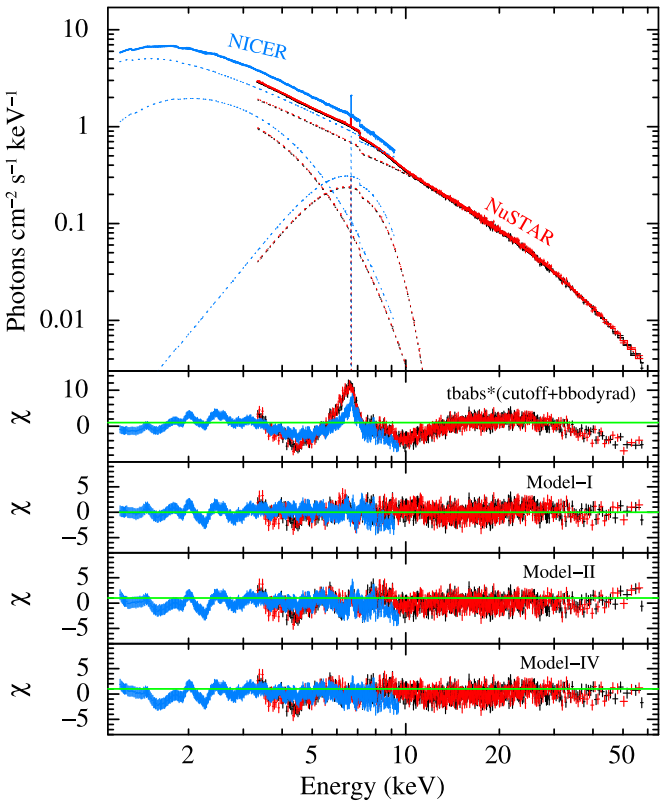

Figure 7. 1.2–79 keV energy spectrum of Swift J0243.6+6124 obtained from quasi-simultaneous *NICER* and *NuSTAR* observations at the peak of the 2017 outburst along with (top and middle panels) the best-fit model comprising a cutoff power-law continuum with a blackbody component, three Gaussian functions, and an edge feature (Model-I). Spectral residuals corresponding to additional models, TBABS*(CUTOFF+BBODYRAD), Model-II: TBABS*(GSMOOTH*COPLREFL+HECUT+BBODYRAD), and Model-IV: TBABS*(RELXILL+CUTOFF+BBODYRAD) are shown in the remaining panels. The cross normalization constant between *NICER* and *NuSTAR* is 1.3 for the brightest observation of the source. The value is obtained with respect to the *NuSTAR*/FPMA detector.

added in the model. This provides a goodness of fit $\chi^2/\nu = 1.14$ for 2556 dof (third panel of Figure 7; Model-I). It is important to note that the addition of the Gaussian components within the Fe band resolved the hump-like residuals that appeared in the Cutoff+BB model fit with a statistical significance of ≈100σ in the χ^2 value. Interestingly, Tao et al. (2019) fitted these wavy features using thermal blackbodies with temperatures of 1.46 and 4.5 keV. In their study, the peaked emissions ($3\,kT_{\rm bb}$) of these thermal components accommodated the Fe-band features that we have identified as lines (see Figure 2 of Tao et al. 2019).

Typically, a reflection spectrum, originating from optically thick material or the accretion disk, peaks at ∼20–30 keV in the form of a prominent broad feature, known as the Compton hump. If the reflection arises from a medium close to the compact object, the strong gravitational field broadens the Fe-line feature and produces a skewed profile (Fabian et al. 2000), as seen in the present study. To account for possible disk reflection in an X-ray pulsar system, we applied the COPLREFL model (Ballantyne et al. 2012) on the absorbed high energy cutoff power-law (HECUT) continuum with a blackbody component in our study. The COPLREFL code generates a reflection spectrum from a constant density disk (10^{19} cm^{-3}) illuminated by a hard power law with a variable high energy

Table 1
Best-fit Spectral Parameters Obtained from Fitting *NICER* and *NuSTAR* Data Close to the Outburst Peak

Model	Parameter	Model-I	Model-II	Model-III	Model-IV
TBABS	$N_{\rm H}$[a]	0.86 ± 0.01	1.67 ± 0.08	1.23 ± 0.02	0.84 ± 0.01
BBODYRAD	kT (keV)	0.85 ± 0.01	1.16 ± 0.04	1.12 ± 0.02	1.12 ± 0.01
	norm	4337 ± 30	886 ± 150	843 ± 32	818 ± 28
POWER-LAW	Γ	1.35 ± 0.01	1.88 ± 0.03	1.61 ± 0.02	1.65 ± 0.01
CUTOFF	$E_{\rm cut}$ (keV)	21.8 ± 0.3	26 ± 2	27.3 ± 0.7	27.2 ± 0.7
	$E_{\rm fold}$ (keV)	⋯	8.2 ± 0.1	⋯	⋯
GAUSSIAN1	E_c (keV)	6.42	⋯	⋯	⋯
	σ (keV)	1.67 ± 0.01	⋯	⋯	⋯
	norm	0.99 ± 0.01	⋯	⋯	⋯
GAUSSIAN2	E_c (keV)	6.67	⋯	⋯	⋯
	σ (keV)	0.05 ± 0.02	⋯	⋯	⋯
	norm	0.02 ± 0.01	⋯	⋯	⋯
GAUSSIAN3	E_c (keV)	6.98	⋯	⋯	⋯
	σ(keV)	0.1	⋯	⋯	⋯
	norm (10^{-4})	2 ± 1	⋯	⋯	⋯
EDGE	Energy (keV)	7.11 ± 0.01	⋯	⋯	⋯
	τ	0.12 ± 0.01	⋯	⋯	⋯
GSMOOTH	$\sigma_{\rm 6keV}$ (keV)	⋯	0.33 ± 0.02	0.19 ± 0.03	⋯
COPLREFL	Γ	⋯	0.87 ± 0.07	⋯	⋯
	log(ξ)	⋯	2.61 ± 0.08	⋯	⋯
	z	⋯	0.0375 ± 0.002	⋯	⋯
	norm (10^{-28})	⋯	2.3 ± 0.6	⋯	⋯
XILLVER	Γ	⋯	⋯	1.18 ± 0.05	⋯
	log(ξ)	⋯	⋯	3.47 ± 0.04	⋯
	$A_{\rm Fe}$	⋯	⋯	5.1 ± 0.3	⋯
	z	⋯	⋯	0.0219 ± 0.003	⋯
	i(°)	⋯	⋯	23^{+28}_{-23}	⋯
	norm (10^{-2})	⋯	⋯	5.0 ± 0.5	⋯
RELXILL	log(ξ)	⋯	⋯	⋯	3.49 ± 0.03
	$A_{\rm Fe}$	⋯	⋯	⋯	4.9 ± 0.3
	z	⋯	⋯	⋯	0.0224 ± 0.007
	i(°)	⋯	⋯	⋯	43^{+25}_{-10}
	$R_{\rm in}$ (R_g)	⋯	⋯	⋯	253^{+237}_{-121}
	$f_{\rm refl}$	⋯	⋯	⋯	$4.0^{+0.2}_{-8}$
	norm (10^{-2})	⋯	⋯	⋯	$1.5^{+3}_{-0.1}$
CFLUX	$F_{\rm refl}$[b]	⋯	0.42 ± 0.01	0.32 ± 0.01	0.43 ± 0.02
	$F_{\rm total}$[b]	1.85 ± 0.01	1.90 ± 0.01	1.88 ± 0.01	1.89 ± 0.01
	χ^2_ν (dof)	1.14 (2556)	1.23 (2564)	1.21 (2563)	1.19 (2562)

Notes. Model-I: tbabs*(cutoff+bbodyrad+ga1+ga2+ga3)*edge, Model-II: tbabs*(gsmooth*Coplrefl+hecut+bbodyrad), Model-III: tbabs*(gsmooth*xillver+cutoff +bbodyrad), and Model-IV: tbabs*(relxill+cutoff+bbodyrad). Uncertainties are reported at the 90% confidence interval and were computed using MCMC (Markov Chain Monte Carlo) of length 100,000.

[a] Equivalent hydrogen column density in 10^{22} cm^{-2}.

[b] The 1–80 keV unabsorbed flux in 10^{-7} erg cm^{-2} s^{-1}. The folding energy $E_{\rm fold}$ is from the high energy cutoff power-law (HECUT) model, while $F_{\rm total}$ and $F_{\rm refl}$ represent the measured total source flux and the flux from the reflection component, respectively. Here, $\sigma_{\rm 6\ keV}$ stands for Gaussian width at 6 keV.

cutoff. This model combination is able to explain the hard X-ray spectral curvature as well as the observed iron line moderately well. The fit improves further by adding a GSMOOTH component subject to Doppler broadening to the COPLREFL code. We then allow the gravitational redshift to vary. The goodness of fit is obtained as $\chi^2/\nu = 1.23$ for 2578 dof with this model (Model-II). We note that the reflection component carries a significant part, approximately 20%, of the source emission. Such a high reflection fraction indicates a larger covering area of reflecting material in close proximity to the X-ray pulsar.

To investigate further, physically motivated new reflection models such as XILLVER (García et al. 2013) and RELXILL (García et al. 2014) were also combined with Cutoff+BB model. These codes assume emission from the inner accretion disk, and are widely used to explore the iron line and reflection components from black holes and weakly magnetized neutron stars in low mass X-ray binaries. We first applied the angle-dependent reflection code, XILLVER with Cutoff+BB model. As the above reflection code assumes a power-law model with a high energy cutoff, the cutoff energy was tied to the cutoff power-law continuum model. This yields a fit with $\chi^2/\nu = 1.29$ for 2564 dof. We then convolved with the GSMOOTH component as follows: `tbabs*(gsmooth*xillver+cutoff+bbodyrad)` (Model-III). This improves the fit with a reduced-χ^2 of 1.21 for 2563 dof. Model-III also rectified the excess residuals at the ends of the 4–8 keV band as seen in the second panel of Figure 7, which also shows how the complex shape of the broad iron line and reflection components affect the energy continuum.

A more self-consistent inner disk-reflection code, RELXILL (García et al. 2014), is used together with the Cutoff+BB base model (Model-IV). The purpose of this model is to test the role of reflection and blurring components in the Fe band. The RELXILL model is the currently most advanced version of reflection code that incorporates XILLVER and a relativistic blurring code RELLINE together. The model components of RELXILL are: emissivity index (q) for the disk, dimensionless spin parameter $a = cJ/GM^2$, inclination angle i (in degrees), the ionization parameter log(ξ), iron abundance with respect to the solar value $A_{\rm Fe}$, and reflection fraction $f_{\rm refl}$, inner disk radius $R_{\rm in}$ in units of gravitational radius R_g (GM/c^2), outer disk radius $R_{\rm out}$ in units of R_g, redshift z, and normalization. We allowed the inner disk radius $R_{\rm in}$ to vary by fixing the outer radius at 990 R_g. The emissivity index for the disk was kept at 3 assuming isotropic point emission (see, e.g., Wilkins 2018). The spin parameter is likely to be $<$0.7 for the range of neutron star masses and radii (Miller et al. 2011), and is considered to be zero in our analysis (Ludlam et al. 2018). The choice of spin value does not affect our results much. We obtained only a difference of 2 R_g in the inner disk radius for the parameter $a = 0$ and $a = 0.7$. The above model approximated the energy continuum well with a goodness of fit $\chi^2/\nu = 1.19$ for 2562 dof (fifth panel of Figure 7).

In this fit, the derived inner disk radius is ≈130–490 R_g from the neutron star. We also detected the gravitational redshift of 0.022 from the reflecting gas, allowing a significant Doppler broadening and redshifted Fe-line profile by ≈6600 km s^{-1}. In general the XILLVER and RELXILL models consider radiation dominated by a classical accretion disk, which may not be realized here. Still, the successful application to the 1.2–79 keV spectrum of Swift J0243.6+6124 indicates strong reflection and gravitational effects in the iron-line band. It is important to mention that the reflection fraction between Model-II, Model-III, and Model-IV is almost the same. It is only possible when the optically thick region is located close to the pulsar and covers substantial central emission.

Best-fitting spectral parameters for Model-I, Model-II, Model-III, and Model-IV are given in Table 1. We also searched for absorption like features that could originate from cyclotron resonance scattering (Jaisawal & Naik 2017; Staubert et al. 2019) in the 1.2–79 keV band. The non-detection of any signature of a cyclotron line in the broadband spectrum could be an indication that the magnetic field of the pulsar is either $>8 \times 10^{12}$ G or $<10^{11}$ G. But at least a low magnetic field is in tension with the magnetic field estimates derived from other methods, as explained in Section 1. Note also that only ∼10% of all known binary X-ray pulsars have an identified cyclotron line feature (Staubert et al. 2019), indicating that additional conditions besides a suitable magnetic field strength are required to form an observable line feature.

4. Discussion

We have analyzed *NICER* observations of the bright transient pulsar during its strong X-ray outburst in late 2017. The neutron star was accreting an order of magnitude above the expected Eddington limit at the outburst peak. The detection of the source at such a high luminosity has established it as the first Galactic ULX pulsar (Tsygankov et al. 2018; Wilson-Hodge et al. 2018). Therefore, the study of Swift J0243.6+6124 provides an opportunity to explore the connection between accretion-powered X-ray pulsars and pulsating ULXs, and also to test theories of super-Eddington accretion.

The present paper reports the detection of iron emission lines in the 6–7 keV range and their evolution with luminosity during the giant outburst of Swift J0243.6+6124. A narrow 6.4 keV line is observed during the sub-Eddington state, as usually seen in other high-mass X-ray binary pulsars (see, e.g., Jaisawal et al. 2016; Jaisawal & Naik 2016). The line-emitting region, in this phase, is probably located relatively far from the neutron star, i.e., in the accretion disk, inside the magnetosphere, or the stellar wind from the companion star. As the luminosity of the pulsar approaches the Eddington limit ($L_{\rm Edd} \approx 1.8 \times 10^{38}$ erg s^{-1} for a 1.4 $M_\odot$ neutron star), the line profile broadens with significant contributions from 6.67 keV (Fe XXV), and 6.97 keV (Fe XXVI) features. A highly asymmetric line profile is observed at luminosities (0.7–1.2) $\times 10^{39}$ erg s^{-1} in the 1–10 keV band of Swift J0243.6+6124 (Figure 2). The ≈6.67 keV emission is found to lead the Fe K band in the ultraluminous state. Weakly magnetized neutron stars or black holes in X-ray binaries, or supermassive black holes in active galactic nuclei, usually show relativistic line profiles from their inner accretion disks in the vicinity of the compact object (see, e.g., Fabian et al. 2000; Miller 2007; Bhattacharyya 2010). The detection of such a broad, skewed line from a magnetized pulsar indicates possible Doppler effects and gravitational redshift at the emission site in the present case.

To investigate the location of the emission sites, the magnetospheric radius, or inner accretion disk radius of the pulsar, is defined as $R_{\rm m} = 1300\, L_{37}^{-2/7}\, M^{1/7}\, R_6^{10/7} B_{12}^{4/7}$ km for disk-accretion (Ghosh & Lamb 1979; Mushtukov et al. 2017), where M is the mass of neutron star in 1.4 $M_\odot$ units, R_6 is the radius in units of 10^6 cm, and B_{12} is the field strength in 10^{12} G units. During the process of accretion, the magnetic field truncates the geometrically thick accretion disk near this point and channels the accreting material onto the neutron star poles. Using the above relation a large magnetosphere is expected at lower luminosities $\leqslant 10^{37}$ erg s^{-1}. It could be ≈5000 km for a highly magnetized pulsar 10^{13} G (see Figure 8). The iron line is possibly produced by the accretion disk, the stellar wind, or from optically thin plasma inside the magnetosphere in the sub-Eddington state.

If we assume a B field upper limit of 10^{13} G and adopt 10^{39} erg s^{-1} as the luminosity of Swift J0243.6+6124, the implied magnetospheric is ≈1300 km from the central object (Figure 8). The accretion disk would not produce a broad relativistic line in this situation. It is possible that the inferred strong magnetic field is dominated by a quadrupolar moment (see, e.g., Bonazzola et al. 2015; Israel et al. 2017a, and references therein), while the dipole is weaker, allowing the disk to come closer to the star. A line-emitting region within 200 km likely carries a relativistic signature from the compact object. The above limit is obtained for a canonical neutron star with spin parameter $a = 0$ by assuming neutral disk reflection (see, e.g., Bardeen et al. 1972; García et al. 2014), and is shown as a shaded area in Figure 8. We note that a lower dipole B field $\leqslant 10^{10}$ G would produce a broad line even at sub- and super-Eddington luminosities, while a more strongly magnetized neutron star, $B \geqslant 10^{12}$ G, truncates the disk beyond 500 km at the Eddington limit. If we assume the observed broad Fe-feature comes from the disk, the dipole B field of the pulsar should be of order 10^{11} G (Figure 8).

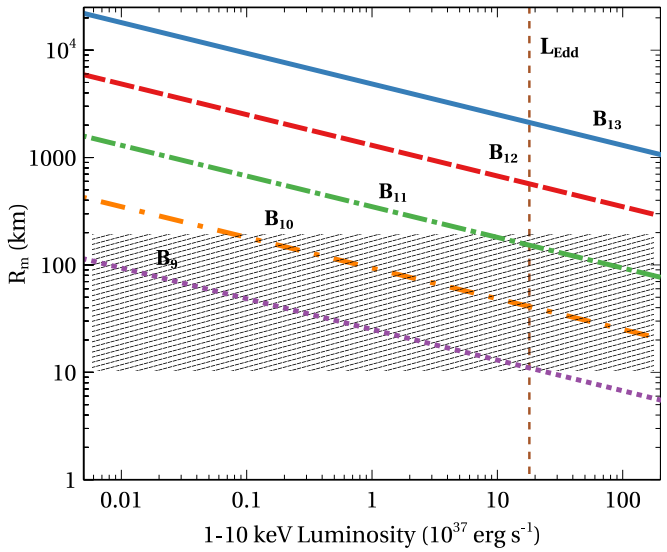

Figure 8. Evolution of the magnetospheric radius (R_m) with luminosity for a range of dipole magnetic fields. Here, B_n denotes the field strength in units of 10^n G. The shaded area presents a zone up to a distance of ≈200 km from a canonical neutron star, allowing a relativistic iron-line profile from the emitting medium due to gravitational effects. We observed a broad Fe line clearly from Swift J0243.6+6124 in the super-Eddington regime. If the line originates from the disk, a possible solution of the pulsar B field can be obtained as an order of 10^{11} G.

The nature of the broad Fe line from Swift J0243.6+6124 in the ultraluminous state is also investigated by using reflection codes, XILLVER and RELXILL. Our modeling suggests that the lines are emitted from a region close to the pulsar, and are subjected to Doppler broadening (0.2 keV) and redshift ($z = 0.022$) which correspond to a net outflow velocity of ≈12,000 km s^{-1}. This is in good agreement with the orbital velocity of the magnetosphere at 1300 km. We note that Model-II predicts a much higher velocity of ≈20,000 km s^{-1}, which is only attainable at a distance of ≈450 km from the X-ray source. Given this rapid flow, the bulk motion of material possibly combined with the gravitational effect near the neutron star gives rise to the broad Fe line. Moreover, it is possible that the receding inner parts of the disk are being illuminated more strongly than the approaching side. This may explain the observed asymmetric line in the super-Eddington state.

Alternative scenarios to describe the pulsar's observed spectral characteristics are possible. Apart from the disk, another possibility of reflecting material around magnetized ULXs is suggested by Mushtukov et al. (2017). The authors find that the optically thin plasma trapped inside the magnetosphere becomes an optically thick curtain (envelope) in the ultraluminous stage ∼10^{39} erg s^{-1}. The photospheric emission from the envelope follows a quasi-thermal spectral shape with temperatures exceeding 1 keV. This envelope is also large enough to reprocess the primary column emission from the neutron star, similar to reprocessing in the disk. In extreme cases, the accretion curtains become thick enough to hide the pulsations, and apparently the ULX spectrum is described by a multicolor blackbody function without the column emission (Mushtukov et al. 2017). The presence of optically thick regions may also lead to the disappearance of cyclotron scattering features from the spectrum (Mushtukov et al. 2017).

Still, the plasma trapped in the magnetosphere remains optically thin closer to the accretion column, producing the emission line features (Koliopanos & Vasilopoulos 2018). The observed broad Fe line from Swift J0243.6+6124 can likely originate from such accreted plasma located next to the star. Nevertheless, theoretical studies of super-Eddington accretion onto black holes or millisecond accreting pulsars also predicts massive ejections of the disk material either in the form of optically thick spherical outflows or optically thin ultrafast winds near the axis of the compact object (Poutanen et al. 2007; Parfrey et al. 2016; Sądowski & Narayan 2016). These optically thin fast-moving outflows in close proximity to the neutron star are also potential sites for broad lines at high accretion phases.

It is important to note that this pulsar launched a jet when the X-ray luminosity was $\geqslant 4 \times 10^{36}$ erg s^{-1} during giant and fainter outbursts (for a distance of 7 kpc; van den Eijnden et al. 2018, 2019). At the same time, the luminosity-dependent emission lines were observed in the spectral range of *NICER*. It is reasonable to consider that the emission lines could originate in a jet because broad Doppler-shifted iron lines have previously been detected from a relativistic 0.26c outflow in SS 433 (Fabrika et al. 2015; Kaaret et al. 2017). The optically thin medium within the jet would also provide the Doppler-shifted emission line, though, a relativistic line profile would appear only if the jet or emission site is located next to the pulsar.

5. Conclusions

In this work, we have studied *NICER* observations of Swift J0243.6+6124 during its 2017–2018 outburst. The 1.2–10 keV energy spectrum from *NICER* can be described by a cutoff power-law model plus Gaussian components for emission lines. We have observed a narrow to broad-line profile from the pulsar during the sub- to super-Eddington states. Depending on the luminosity, the Fe band contained up to three emission lines of energies ≈6.4, 6.7, and 6.98 keV from neutral and highly ionized Fe-atoms. We have also shown that the iron line is relatively complex in the ultraluminous state, affecting the continuum spectrum and the choice of spectral modeling. Tao et al. (2019) have described the 3–79 keV energy spectrum in the super-Eddington state with a cutoff power-law model with three blackbody components. With the inclusion, instead, of lines in the model and the soft X-ray coverage of *NICER*, the 1.2–79 keV energy spectrum in this state is well described by a similar cutoff power law plus blackbody model as used for the pulsar in the low luminosity state. We have shown that the two additional blackbody components used by Tao et al. (2019) are not required at extreme luminosity as long as the iron-line complex is modeled carefully.

Our analysis suggests that emission lines observed in sub-Eddington regimes mainly originate far from the pulsar. It could be hosted by the accretion disk, the plasma trapped in the magnetosphere, optically thin ejected material or in the jet outflow. We clearly observed evolution of the line profile with luminosity in terms of the number of line constituents and their breadth, which suggests that the emission site was evolving across the outburst. In the beginning, these sites were located at a distance of ∼5000 km (for a luminosity of 10^{37} erg s^{-1}) and moved much closer to the neutron star during the ultraluminous phase. The detection of an asymmetric broad iron line at this stage also indicates the presence of Doppler effects and gravitational redshift. The possibility of a broad line from the disk can be considered only if the neutron star possesses a

dipolar B field strength in the narrow range between 10^{11} and 10^{12} G. The observed line in the super-Eddington state may also originate from an optically thin accretion curtain, an ultrafast plasma, or in the jet close to the compact object.

We sincerely thank the referee for useful suggestions on the paper. This work was supported by NASA through the *NICER* mission and the Astrophysics Explorers Program, and made use of data and software provided by the High Energy Astrophysics Science Archive Research Center (HEASARC). This project has received funding from the European Union's Horizon 2020 research and innovation programme under the Marie Skłodowska-Curie grant agreement No. 713683. A.L.S. is supported by an NSF Astronomy and Astrophysics Postdoctoral Fellowship under award AST-1801792. D.A. acknowledges support from the Royal Society. R.M.L. acknowledges the support of NASA through Hubble Fellowship Program grant HST-HF2-51440.001.

Facilities: ADS, HEASARC, *NICER*, *NuSTAR*, *Swift*.

Software: HEASOFT (v6.24), XSPEC (v12.10.0; Arnaud 1996), COPLREFL (Ballantyne et al. 2012), XILLVER (García et al. 2013), RELXILL (García et al. 2014), Veusz.

ORCID iDs

Gaurava K. Jaisawal https://orcid.org/0000-0002-6789-2723
Colleen A. Wilson-Hodge https://orcid.org/0000-0002-8585-0084
Andrew C. Fabian https://orcid.org/0000-0002-9378-4072
Sachindra Naik https://orcid.org/0000-0003-2865-4666
Deepto Chakrabarty https://orcid.org/0000-0001-8804-8946
Peter Kretschmar https://orcid.org/0000-0001-9840-2048
David R. Ballantyne https://orcid.org/0000-0001-8128-6976
Renee M. Ludlam https://orcid.org/0000-0002-8961-939X
Jérôme Chenevez https://orcid.org/0000-0002-4397-8370
Diego Altamirano https://orcid.org/0000-0002-3422-0074
Felix Fürst https://orcid.org/0000-0003-0388-0560
Sebastien Guillot https://orcid.org/0000-0002-6449-106X
Christian Malacaria https://orcid.org/0000-0002-0380-0041
Michael T. Wolff https://orcid.org/0000-0002-4013-5650

References

Arnaud, K. A. 1996, in ASP Conf. Ser. 101, Astronomical Data Analysis Software and Systems V, ed. G. H. Jacoby & J. Barnes (San Francisco, CA: ASP), 17
Bachetti, M., Harrison, F. A., Walton, D. J., et al. 2014, Natur, 514, 202
Bahramian, A., Kennea, J. A., & Shaw, A. W. 2017, ATel, 10866, 1
Ballantyne, D. R., Purvis, J. D., Strausbaugh, R. G., & Hickox, R. C. 2012, ApJL, 747, L35
Bardeen, J. M., Press, W. H., & Teukolsky, S. A. 1972, ApJ, 178, 347
Bhattacharyya, S. 2010, AdSpR, 45, 949
Bikmaev, I., Shimansky, V., Irtuganov, E., et al. 2017, ATel, 10968, 1
Bildsten, L., Chakrabarty, D., Chiu, J., et al. 1997, ApJS, 113, 367
Bonazzola, S., Mottez, F., & Heyvaerts, J. 2015, A&A, 573, A51
Cenko, S. B., Barthelmy, S. D., D'Avanzo, P., et al. 2017, GCN, 21960, 1
Doroshenko, V., Tsygankov, S., & Santangelo, A. 2018, A&A, 613, A19
Fabian, A. C., Iwasawa, K., Reynolds, C. S., & Young, A. J. 2000, PASP, 112, 1145
Fabian, A. C., Rees, M. J., Stella, L., & White, N. E. 1989, MNRAS, 238, 729
Fabrika, S., Ueda, Y., Vinokurov, A., Sholukhova, O., & Shidatsu, M. 2015, NatPh, 11, 551
Fender, R. 2006, in Jets from X-Ray Binaries, ed. W. H. G. Lewin & M. van der Klis (Cambridge: Cambridge Univ. Press), 381
Fürst, F., Walton, D. J., Harrison, F. A., et al. 2016, ApJL, 831, L14
García, J., Dauser, T., Lohfink, A., et al. 2014, ApJ, 782, 76
García, J., Dauser, T., Reynolds, C. S., et al. 2013, ApJ, 768, 146
Gendreau, K. C., Arzoumanian, Z., & Okajima, T. 2012, Proc. SPIE, 8443, 13
Gendreau, K. C., Arzoumanian, Z., Adkins, P. W., et al. 2016, Proc. SPIE, 9905, 99051H
Ghosh, P., & Lamb, F. K. 1979, ApJ, 234, 296
Harrison, F. A., Craig, W. W., Christensen, F. E., et al. 2013, ApJ, 770, 103
Israel, G. L., Belfiore, A., Stella, L., et al. 2017a, Sci, 355, 817
Israel, G. L., Papitto, A., Esposito, P., et al. 2017b, MNRAS, 466, L48
Jahoda, K., Markwardt, C. B., Radeva, Y., et al. 2006, ApJS, 163, 401
Jaisawal, G. K., & Naik, S. 2016, MNRAS, 461, L97
Jaisawal, G. K., & Naik, S. 2017, in 7 Years of MAXI: Monitoring X-Ray Transients, ed. M. Serino et al. (Saitama: Riken), 153
Jaisawal, G. K., Naik, S., & Chenevez, J. 2018, MNRAS, 474, 4432
Jaisawal, G. K., Naik, S., & Epili, P. 2016, MNRAS, 457, 2749
Jenke, P., & Wilson-Hodge, C. A. 2017, ATel, 10812, 1
Kaaret, P., Corbel, S., Prestwich, A. H., & Zezas, A. 2003, Sci, 299, 365
Kaaret, P., Feng, H., & Roberts, T. P. 2017, ARA&A, 55, 303
Kara, E., Steiner, J. F., Fabian, A. C., et al. 2019, Natur, 565, 198
Kennea, J. A., Lien, A. Y., Krimm, H. A., Cenko, S. B., & Siegel, M. H. 2017, ATel, 10809, 1
King, A., & Lasota, J.-P. 2019, MNRAS, 485, 3588
King, A. R. 2009, MNRAS, 393, L41
Koliopanos, F., & Vasilopoulos, G. 2018, A&A, 614, A23
Krimm, H. A., Holland, S. T., Corbet, R. H. D., et al. 2013, ApJS, 209, 14
Ludlam, R. M., Miller, J. M., Arzoumanian, Z., et al. 2018, ApJL, 858, L5
Massi, M., & Kaufman Bernadó, M. 2008, A&A, 477, 1
Middleton, M. J., Heil, L., Pintore, F., Walton, D. J., & Roberts, T. P. 2015, MNRAS, 447, 3243
Miller, J. M. 2006, AN, 327, 997
Miller, J. M. 2007, ARA&A, 45, 441
Miller, J. M., Gendreau, K., Ludlam, R. M., et al. 2018, ApJL, 860, L28
Miller, J. M., Miller, M. C., & Reynolds, C. S. 2011, ApJL, 731, L5
Mushtukov, A. A., Suleimanov, V. F., Tsygankov, S. S., & Ingram, A. 2017, MNRAS, 467, 1202
Parfrey, K., Spitkovsky, A., & Beloborodov, A. M. 2016, ApJ, 822, 33
Poutanen, J., Lipunova, G., Fabrika, S., Butkevich, A. G., & Abolmasov, P. 2007, MNRAS, 377, 1187
Prigozhin, G., Gendreau, K., Foster, R., et al. 2012, Proc. SPIE, 8453, 845318
Protassov, R., van Dyk, D. A., Connors, A., Kashyap, V. L., & Siemiginowska, A. 2002, ApJ, 571, 545
Sądowski, A., & Narayan, R. 2016, MNRAS, 456, 3929
Staubert, R., Trümper, J., Kendziorra, E., et al. 2019, A&A, 622, A61
Tao, L., Feng, H., Zhang, S., et al. 2019, ApJ, 873, 19
Tsygankov, S. S., Doroshenko, V., Mushtukov, A. A., Lutovinov, A. A., & Poutanen, J. 2018, MNRAS, 479, L134
van den Eijnden, J., Degenaar, N., Russell, T. D., et al. 2018, Natur, 562, 233
van den Eijnden, J., Degenaar, N., Russell, T. D., et al. 2019, MNRAS, 483, 4628
White, N. E., Swank, J. H., & Holt, S. S. 1983, ApJ, 270, 711
Wilkins, D. R. 2018, MNRAS, 475, 748
Wilms, J., Allen, A., & McCray, R. 2000, ApJ, 542, 914
Wilson-Hodge, C. A., Malacaria, C., Jenke, P. A., et al. 2018, ApJ, 863, 9